Sensorless Saliency-Based Control of Dual Induction Machines Under Dynamic Load Imbalances Using Three Current Sensors

Eduardo Rodriguez Montero, *Student Member, IEEE*, Markus Vogelsberger, and Thomas Wolbank, *Member, IEEE*

***Abstract*—To perform vector control of single-inverter dual induction motors, drives are standardly equipped with current and position sensors. In medium-power railway applications, a shaft encoder is usually mounted on each motor, and the inverter output current is measured using two current sensors. Yet, this configuration features some disadvantages. First, torque-sharing cannot be computed because stator current of each motor is unknown. Similarly, saliency extraction of each motor is not achievable since individual current drawn by each motor is not measured. An option that achieves torque-sharing calculation is to attach two current sensors to each motor, provided that both rotor positions are known. However, industrial inverter/control platforms considered offer a maximum of three input channels for current sensors. Besides, some industry fields tend towards encoderless speed control. Therefore, this article proposes to use three current sensors in total and no shaft encoders. Thanks to a special current sensor arrangement and a voltage step excitation method, saliency-based encoderless control is achieved. In addition, a method is presented to estimate torque-sharing. Experimental measurements, taken on a dual induction motor test bench, will show the capability of the proposed methodology to identify individual loading as well as excellent encoderless control performance.**

***Index Terms*—Angular velocity control, harmonic analysis, induction motor, sensorless control, signal processing algorithms.**

I. Introduction

THE parallel supply of dual induction motors by a single inverter is an attractive practice due to its low cost, reduced size, and decreased maintenance needs. If both induction motors and their speeds were identical, the parallel condition would result in identical torque levels in each machine. However, this does not occur in railway applications due to some factors, such as unequal wheel diameter, driving in a curve, or sudden wheel slipping [1]. In addition, motor parameters may differ to some extent. In this sense, motors operate typically under unequal load. Unawareness of torque-sharing and machine speed may lead to instabilities and decreased drive performance [2]. Therefore, accurate acquisition of torque-sharing and machine speed may be crucial to ensure stable operation under heavy load imbalances. Yet, the ability of the control structure to calculate flux and torque-sharing depends on the selected sensor configuration, regarding both current and position sensors.

It is possible to attach two current sensors in total at two inverter output phases, and attach a position sensor to each motor. This configuration is widespread in medium-power railway applications. Vector control strategies, such as field oriented control (FOC) or direct torque control that use this sensor configuration often assume a symmetrical distribution of torque and flux since only sum current of both motors is available. Consequently, torque-sharing is not identifiable, which can worsen drive performance [2].

By attaching two current sensors at two phases of each machine and having a position signal of each machine, flux, and torque-sharing can be identified. This information has been used in literature to increase drive robustness and stability by adjusting the flux magnitude in case of load imbalances [2], [3], [4].

Alternatively, this article proposes to use three current sensors as in [15] (two attached to the first motor "*M1*" and one to the second "*M2*"). A method will be presented to calculate the flux and torque of each motor despite the reduced amount of current sensors in the drive.

In addition, this article will calculate the rotor position without the need of any position sensor, with special focus to the proximity to zero frequency. In this speed region, fundamental-wave models and observers become unstable due to parameter uncertainty and inverter nonlinearities. Such models have been deeply investigated in the context of encoderless dual motor drives [5], [6], [7]. However, saliency extraction can provide meaningful information in the very low speed region [12], using either high

Manuscript received 20 April 2022; revised 26 July 2022, 22 September 2022, and 21 December 2022; accepted 31 December 2022. Date of publication 2 February 2023; date of current version 9 June 2023. This work was supported by ALSTOM-Rolling Stock Platform/Components Division-Bogies & DRIVES Department for Research/Development funding. *(Corresponding author: Eduardo Rodriguez Montero.)*

Eduardo Rodriguez Montero and Thomas Wolbank are with the Technical University of Vienna, 1040 Vienna, Austria (e-mail: eduardo.montero@tuwien.ac.at; thomas.wolbank@tuwien.ac.at).

Markus Vogelsberger is with the Rolling Stock Platform/Components Division—DRIVES, ALSTOM Transport Austria GmbH, 1220 Vienna, Austria (e-mail: markus.vogelsberger@alstomgroup.com).

Color versions of one or more figures in this article are available at https://doi.org/10.1109/TIE.2023.3241394.

Digital Object Identifier 10.1109/TIE.2023.3241394

frequency injection [8], [9], [10] or voltage step excitation [11], [12], [13], [14], [15], [16].

In this article, rotor-slotting saliency (also named slotting saliency in this article) will be extracted for encoderless control using voltage step excitation. Voltage steps are applied through inverter switching in order to calculate the resulting phase current slopes. Since saliencies are reflected at the transient leakage inductance, calculated current slopes contain the desired information about the saliencies. Two different signal processing methods are used, since the current sensors are not symmetrically arranged (two in first motor and one in the second). Besides, since both machines exhibit multiple saliencies, feedforward saliency compensation is used [11]. Each noncontrol-saliency signal is identified for some torque and flux levels and stored in a look-up table (LUT) that is accessed during online operation. The result is a rotor-slotting saliency signal for each machine that is transformed into a rotor position given the rotor slot number.

The proposed torque-sharing calculation method and rotor slotting extraction method are implemented on a single-inverter dual 11 kW motor test stand using the proposed three current sensor arrangement and the voltage step excitation of [15]. To extract rotor-slotting saliency, a feedforward compensation method is used, which requires flux and torque of both *M1* and *M2*. Besides, a new technique to compute individual torque and flux level is presented. Experimental results show accurate torque and flux calculation under dynamic operation as well as excellent rotor position acquisition based on the rotor-slotting saliency of both motors at unbalanced dynamic load operation.

II. Control of Dual Induction Motor Drives

In dual induction motor drives, two induction machines are connected in parallel and supplied by a single inverter. It is a common practice in several industry applications such as traction drives for rolling stocks. Dual motor drives present less weight, volume and cost compared to the standard drive where one inverter feeds a single motor.

A. Vector Control

For applications where high-performance dynamic operation is required, vector control is often used. One of the most used vector control methods is called FOC and relies on decoupled current control in a coordinate system that is fixed to the rotor flux angle. The x-axis points in the direction of the rotor flux angle and the y-axis is 90° shifted. The motor model involved in FOC is usually the so-called inverse-Γ motor model. It is shown in Fig. 1.

Where R_S is stator resistance, i_S stator current, U_S stator voltage, L_σ leakage inductance, L_μ magnetizing inductance, and R_R rotor resistance. Ψ denotes flux.

The rotor flux equation becomes as in (1) when rotor-fixed coordinates are used

$$\dot{\underline{\psi}}_R = R_R / L_\mu \cdot \left(-\underline{\psi}_R + L_\mu \cdot \underline{i_S} \right). \tag{1}$$

As seen in (1), rotor flux can be calculated from the stator currents and rotor position. By controlling the x and y current components, rotor flux ψ_R and torque T can be indirectly controlled as

$$|\psi_R| = L_\mu \cdot i_{Sx} \tag{2}$$

$$T = i_{Sy} \cdot |\psi_R| . \tag{3}$$

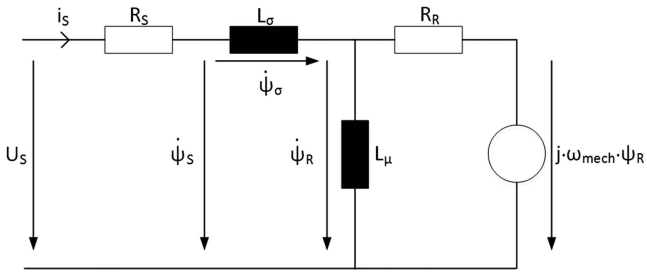

Fig. 1. Inverse-Γ induction motor model.

In this article, rotor flux and torque are estimated using (1)–(3) for each motor individually to allow estimation of torque-sharing. The flux and torque current components (x–y) of each motor are averaged and used for the common FOC.

B. Typical Current Sensor Configurations

The simplest and most economical current sensor configuration, in the field of dual motors, relies on two current sensors placed at two inverter output phases. They measure the sum current since motors are switched in parallel. Therefore, this configuration assumes that both motors are equal and does not allow torque-sharing calculation. Having information on the torque-sharing can improve drive stability and performance [1], [2], [3], [4]. Xu et al. [1], [3] utilize a weighing factor to relieve torque difference. Xu et al. [2] utilizes a weighting factor to shift the control towards most-loaded motor in order to improve dynamic response. Bouscayrol et al. [4] employs a weighting factor to improve speed performance under load imbalances.

C. Proposed Current Sensor Configuration

In this article, a configuration consisting of three current sensors is proposed [18]. As shown in Fig. 2, sensors 1 and 2 measure phase currents A and B of *M1* (depicted in red) and sensor 3 measures phase current C of *M2* (depicted in blue).

Note that, in Fig. 2, each motor is represented by a simplified transient model, characterized by three parameters. This model will be used later for pulse excitation. R_S is the stator resistance, L is the transient leakage inductance, and E back EMF induced by fundamental-wave currents. The three motor phases are indexed with letter ABC. Within the inverter, the eight switching states for a two-level three-phase inverter are represented in three-bit notation.

III. Stator Current Phasor Acquisition

A. Motor M1

Considering the sensor arrangement of Fig. 2 and assuming a balanced three-phase system, the stator current phasor of *M1*

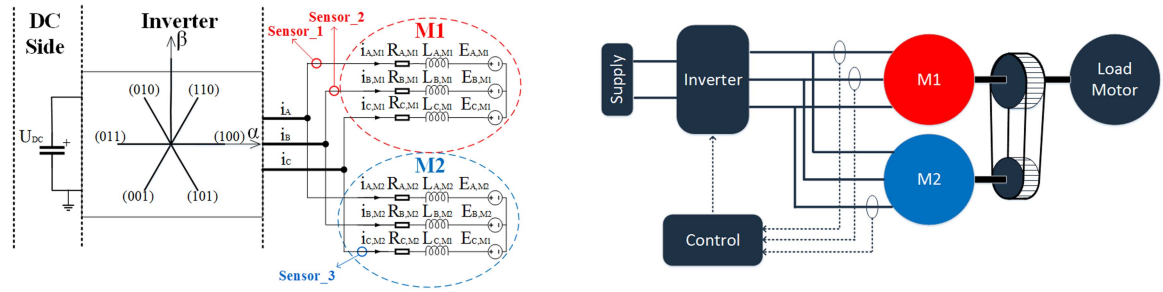

Fig. 2. Left: DC link-inverter-dual motor schematic representation. Right: Test stand set-up block diagram with control and measuring equipment.

can be calculated as usual by means of sensor_1 and sensor_2. Phase C current $i_{C,M1}$ and the stator current phasor $\bar{i}_{S,M1}$ can be calculated as in (4), (5), a being $e^{j2\pi/3}$

$$i_{C,M1} = -i_{A,M1} - i_{B,M1} \tag{4}$$

$$\bar{i}_{S,M1} = i_{A,M1} + i_{B,M1} \cdot a + i_{C,M1} \cdot a^2. \tag{5}$$

B. Motor M2

In this motor, only phase C current is measured. This article presents a signal processing that obtains the stator current phasor of *M2* with the given reduced amount of sensors. As sensor_3 is available, and considering (4), a factor that links both stator currents is derived.

Sinusoidal current is assumed, leading to

$$i_{C,M1} = I_{C,M1} \cdot \sin\left(w_{e,M1} \cdot t + \delta_{C,M1}\right) \tag{6}$$

$$i_{C,M2} = I_{C,M2} \cdot \sin\left(w_{e,M2} \cdot t + \delta_{C,M2}\right) \tag{7}$$

where I is the sinusoid amplitude, w_e electrical frequency, and δ phase shift. Assuming unbalanced load or nonidentical parallel motors, (8)–(10) hold true

$$I_{C,M1} \neq I_{C,M2} \tag{8}$$

$$\delta_{C,M1} \neq \delta_{C,M2} \tag{9}$$

$$w_{e,M1} = w_{e,M2}. \tag{10}$$

Due to the parallel connection, the electrical speed of both currents is equal and the factor $\bar{k}$ can be defined as a polar variable

$$\bar{k} = \frac{I_{C,M2} \cdot e^{i \cdot \delta_{C,M2}}}{I_{C,M1} \cdot e^{i \cdot \delta_{C,M1}}} = \frac{I_{C,M2}}{I_{C,M1}} \cdot e^{j \cdot (\delta_{C,M2} - \delta_{C,M1})}. \tag{11}$$

Once $\bar{k}$ is acquired, since $\bar{i}_{S,M1}$ is known, $\bar{i}_{S,M2}$ can be calculated as

$$\bar{i}_{S,M2} = \bar{i}_{S,M1} \cdot \bar{k}. \tag{12}$$

C. Block Diagram

This section describes the method used for calculating $\bar{k}$. The block diagram of the calculation is shown in Fig. 3, together with the average FOC control scheme and encoderless rotor angle extraction. A phase-locked loop (PLL) is used for calculating and filtering the electrical speed, as well as for calculating the electrical wave period (equal for both motors). The PLL receives the angle of the stator current phasor of *M1* (θ_e) as this phasor can be straightforward calculated using (4) and (5). The block diagram of the PLL is shown in Fig. 4. PD denotes phase detector, which is implemented as $\sin(\theta_e - \hat{\theta}_e)$.

Since the critical speed range for encoderless control is around standstill, up to a few Hz, k_p and k_i are chosen to produce a time constant of 50 ms for a 0→5 Hz frequency step.

To calculate the phase shift difference of (11), in contrast to the PLL of [18], a zero crossing detector is implemented for each motor, which requires less computational resources. Note that, for the calculation of $\bar{k}$, only angle difference is required, and not the individual phase shifts. The calculation is carried out using the number of samples per period of the estimated speed and the samples passed between the zero crossings.

The amplitude of the *C* current wave is calculated by estimating its maximum and minimum. After $\bar{k}$ is estimated, the current phasor of each motor is sent to the motor flux and torque estimator based in (1)–(3). At electrical standstill, torque-sharing can be calculated using mechanical speed difference of both motors. However, this falls outside the topic of this article. In this article, it is preferable to shift control from average FOC towards FOC of *M1* (where two current sensors are available) during electrical standstill.

As stated in (1)–(3), the rotor position is needed for flux and torque calculation. In this article, encoderless control based on pulse excitation is used.

IV. Voltage-Pulse-Based Rotor Position Detection of Dual Motors

A. IM Saliencies

The machine geometric and magnetic construction characteristics define the inherent machine saliencies. Due to these asymmetries, a deterministic modulation of the air-gap flux occurs, which contains information about the rotor magnetic and mechanical position. This effect is reflected in the transient leakage inductances L_A, L_B, L_C (see Fig. 2), which can be evaluated thanks to the stator voltage equation. For an arbitrary motor phase N, (13) holds true

$$(U_N - R_{S,N} \cdot i_N - E_N) \cdot 1/L_N = di_N/dt \tag{13}$$

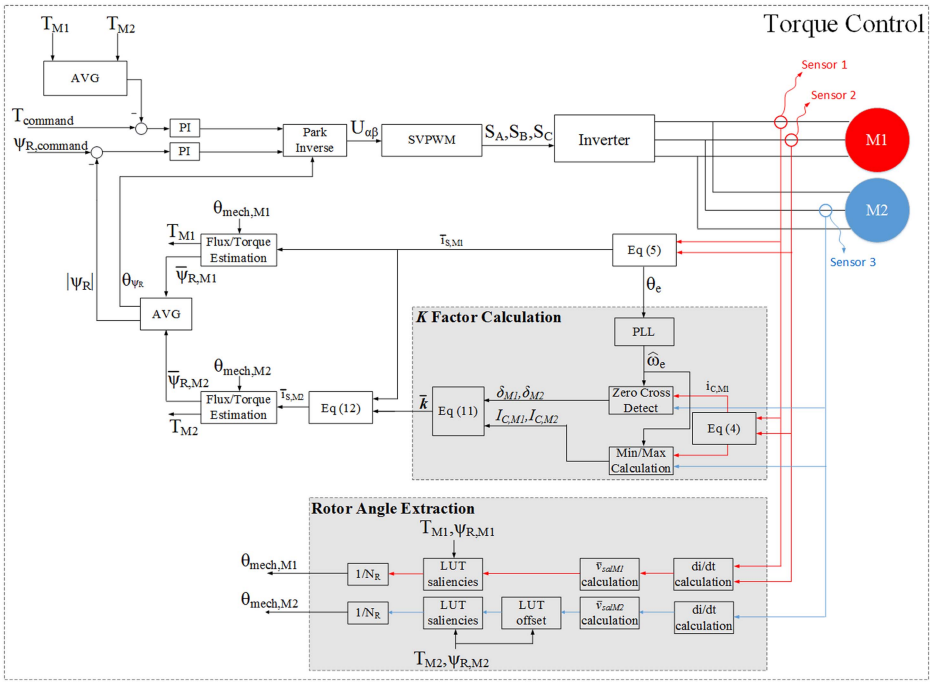

Fig. 3. Average FOC, $\bar{k}$ factor calculation technique and encoderless rotor angle extraction.

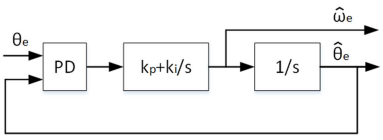

Fig. 4. PLL structure.

TABLE I
SATURATION, SLOTTING, AND INTERMODULATION FUNDAMENTAL-WAVE SALIENCY ANGLES

	$\gamma_{m,sat}$	$\gamma_{m,slot}$	$\gamma_{m,inter}$
γ_m	$2 \cdot \theta_e$	$-N_R \cdot \theta_{mech}$	$N_R \cdot \theta_{mech} - 2 \cdot \theta_e$

The transient leakage inductance of (13) can be described as in (14)–(16), considering N_sal saliencies present in the motor

$$L_A(\gamma_m) = L_0 + \sum_{n=1}^{N\_sal} L_m \cdot \sin(\gamma_m) \tag{14}$$

$$L_B(\gamma_m) = L_0 + \sum_{n=1}^{N\_sal} L_m \cdot \sin(\gamma_m + 2 \cdot \pi/3) \tag{15}$$

$$L_C(\gamma_m) = L_0 + \sum_{n=1}^{N\_sal} L_m \cdot \sin(\gamma_m + 4 \cdot \pi/3) \tag{16}$$

where L_0 denotes the transient leakage inductance offset, and $L_m \cdot \sin(\gamma_m)$ one sinusoid originated by this single saliency, L_m being saliency amplitude, and γ_m saliency angle.

In induction motors, certain designs can lead to the appearance of several spatial saliencies. They appear superposed in the transient leakage inductance defined in (14)–(16).

The most common saliencies in induction motors are the magnetic saturation and rotor-slotting. The magnetic saturation is caused by the local saturation of the leakage paths due to the fundamental wave flux, and the fundamental-wave angle $\gamma_{m,\text{sat}}$ is proportional to the electrical angle θ_e. Rotor-slotting saliency is caused by the effective air-gap length variation due to the rotor bars, and its fundamental-wave angle $\gamma_{m,\text{slot}}$ is proportional to the mechanical angle θ_{mech}. In addition, a third saliency will be considered, originated by the interaction of the saturation and slotting, and often named intermodulation. As a result, intermodulation fundamental-wave angle $\gamma_{m,\text{inter}}$ is proportional to the electrical and mechanical angle. The exact formulation for the fundamental-wave angle of the considered saliencies is given in Table I.

Where N_R represents the amount of rotor slots.

B. Saliency Extraction Using Voltage Pulses

As (13) shows, the phase current derivative is directly related to the transient leakage inductance if the stator resistance voltage drop and back EMF are eliminated, assuming a constant dc-link voltage. In this article, current slopes are calculated using least-square linear regression method [10]. Moreover, as formulated in (14)–(16), the phase transient leakage inductance reflects the effect of the motor saliencies. To eliminate the stator resistance voltage drop and back EMF from (13), a phase current slope difference originated from two different voltage steps is often done [15]. In this sense, after two different voltage steps are applied through the inverter, the resulting current slope difference delivers information on the transient leakage inductance, where motor saliencies are reflected.

In this article, given the sensor arrangement of Fig. 2, only phase C current is available at *M2*, while A and B currents are available at *M1*. Therefore, two different saliency vectors are obtained, one for each motor.

The switching sequence used for machine excitation in this article consists of the three sets of antiparallel inverter states: (100&011, 010&101, and 001&110).

C. M1 Saliency Vector

In order to transform phase current slopes into a saliency vector, a combination of the estimated current slopes can be carried out. Phase-C current is obtained as in (4). An example of phase current slope vector combination is shown in (17) and (18) for excitation with 100 and 011 inverter states

$$\begin{aligned} di_{M1}^{100} - di_{M1}^{011} = & \frac{di_{A,M1}^{(100)}}{dt} - \frac{di_{A,M1}^{(011)}}{dt} \\ & + \left(\frac{di_{B,M1}^{(100)}}{dt} - \frac{di_{B,M1}^{(011)}}{dt} \right) \cdot e^{i\left(2\cdot\frac{\pi}{3}\right)} \\ & + \left(\frac{di_{C,M1}^{(100)}}{dt} - \frac{di_{C,M1}^{(011)}}{dt} \right) \cdot e^{i\left(4\cdot\frac{\pi}{3}\right)}. \end{aligned} \quad (17)$$

In the same way, $di_{M1}^{010} - di_{M1}^{101}$ and $di_{M1}^{001} - di_{M1}^{110}$ are also calculated from the three phase current slopes.

Finally, for *M1*, an offset-less saliency vector $\bar{v}_{\text{sal},M1}$ is created. Due to the signal processing of (17), (18), the effect of the transient leakage inductance offset L_0 (which results from the symmetrical machine only) is mathematically compensated. Note that, in (18) only one single saliency L_m is represented for clarity reasons

$$\begin{aligned} \bar{v}_{sal,M1} = & \, di_{M1}^{100} - di_{M1}^{011} \\ & + \left(di_{M1}^{010} - di_{M1}^{101}\right) \cdot e^{i\left(2\cdot\frac{\pi}{3}\right)} \\ & + \left(di_{M1}^{001} - di_{M1}^{110}\right) \cdot e^{i\left(4\cdot\frac{\pi}{3}\right)} \\ = & \, -3 \cdot L_m \cdot e^{i\cdot(\gamma_{m,M1})} \cdot \text{cst} \end{aligned} \quad (18)$$

where the term cst is

$$\text{cst} = U_{\text{DC}} \cdot \left(L_0^2 - 1/4 \cdot L_m^2\right)^{-1}. \quad (19)$$

D. M2 Saliency-Offset Vector

The signal processing used for *M2* as well as the output differs from those of *M1* since *M2* is only equipped with one current sensor, attached at phase C. Under 100 and 011 voltage steps, the phase current difference of (20) is done

$$di_{M2}^{100} - di_{M2}^{011} = \left(\frac{di_{C,M2}^{(100)}}{dt} - \frac{di_{C,M2}^{(011)}}{dt} \right). \quad (20)$$

In the same way, $di_{M2}^{010} - di_{M2}^{101}$ and $di_{M2}^{001} - di_{M2}^{110}$ are also calculated from the *C* current slope scalar subtraction used in (18). A vector sum of the resulting C current slope differences is further performed in (21) to transform saliencies into a vector

$$\begin{aligned} \bar{v}_{sal,M2} = & \left(di_{M1}^{100} - di_{M1}^{011}\right) \cdot e^{i\left(5\cdot\frac{\pi}{6}\right)} \\ & + \left(di_{M1}^{010} - di_{M1}^{101}\right) \cdot e^{i\left(9\cdot\frac{\pi}{6}\right)} \\ & + \left(di_{M1}^{001} - di_{M1}^{110}\right) \cdot e^{i\left(1\cdot\frac{\pi}{6}\right)} \\ = & \left(2 \cdot L_0 \cdot e^{i\left(\frac{\pi}{6}\right)} - L_m \cdot e^{i\cdot(\gamma_{m,M1})}\right) \cdot \text{cst}. \end{aligned} \quad (21)$$

As observed in (21), the reduced amount of current sensors in M2 leads to a vector where the effect of the transient leakage inductance offset L_0 appears superposed to the saliency L_m.

E. Offset Elimination

In order to access saliencies, the offset of the saliency vector must be previously eliminated. *M1* saliency vector has no offset, as seen in (18). However, the saliency vector of *M2* contains an offset whose amplitude varies depending on the actual flux and torque in the motor. In induction motors, the transient leakage inductance offset is many tens of times bigger than the amplitude of the saliencies. Therefore, accurate compensation must be performed.

In this article, the offset is estimated during a commissioning for multiple flux and torque levels using a mean function on the saliency vector $\bar{v}_{\text{sal},M2}$ stored for several electrical revolutions. The result is a three-dimensional LUT which outputs the actual vector offset at a given torque and flux, named "LUT offset" in Fig. 3. Offset is feedforward compensated.

F. Saliency Separation

After eliminating the vector offset, a signal containing only motor saliencies superposed remains. It is then the task of the saliency separation scheme to compensate all motor saliency harmonics from the saliency vector except one, from which the rotor information will be extracted. In this article, the slotting saliency is used as the feedback control signal, as it can directly be transformed into a rotor position given the rotor slot number.

As with the offset, saliencies are estimated during a commissioning for multiple flux and torque levels using a cost function as explained in [13]. The noncontrol saliencies are feedforward compensated during normal operation using the "LUT saliencies" of Fig. 3. In contrast to [15], saliencies and offset of $\bar{v}_{\text{sal},M1}$ and $\bar{v}_{\text{sal},M2}$ are evaluated not only at different torque levels, but also difference flux levels.

G. Block Diagram

The block diagram of the encoderless saliency-based rotor position extraction is shown in Fig. 3. As observed, initially the current slopes are estimated. In this article, linear regression with 2 MS/s sampling is employed. These current slopes are combined as described in Section IV-C and Section IV-D, leading to $\bar{v}_{\text{sal},M1}$ and $\bar{v}_{\text{sal},M2}$. After offset elimination and saliency separation, the rotor-slotting saliency remains, from which the rotor position is calculated knowing the rotor slot number N_R.

TABLE II
MOTOR AND BELT PARAMETERS

M1 and M2	Voltage (V)	280
	Current (A)	30.5
	Frequency (Hz)	75
	Power (kW)	13.8
	Speed (r/min)	2180
Toothed belt wheels	Wheel_M1 (mm)	40
	Wheel_M2 (mm)	55

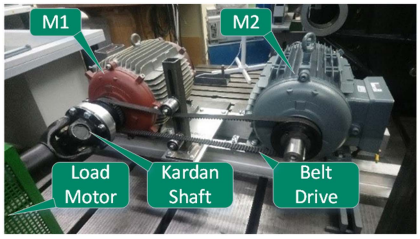

Fig. 5. Test stand used during experimental tests.

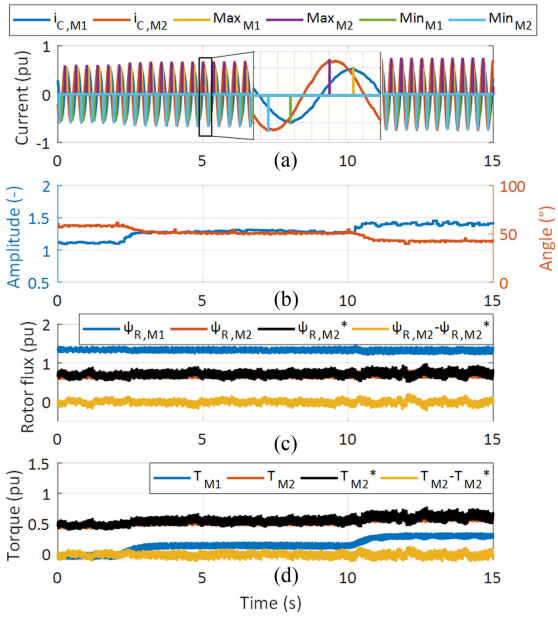

Fig. 6. (a) Phase C current in both motors and detected max/min. (b) $\bar{k}$ factor regarding amplitude and angle, calculated as in (11). (c) Calculated *M1* and *M2* rotor flux using proposed current sensor configuration (blue and red). *M2* flux using two current sensors, attached for comparison reasons, is also shown. (d) Calculated M1 and *M2* rotor torque using proposed current sensor configuration (blue and red). *M2* torque using two current sensors, attached for comparison reasons, is also shown.

V. TEST STAND DESCRIPTION

A. Electrical Parameters

The drive consists of a single insulated gate bipolar transistor (IGBT)-based inverter that supplies two four-pole parallel-connected induction motors whose design was chosen as identical as possible. There are, however, still some small deviations between the parameters of each motor. Each rotor is unskewed. The stator slot number is 36 and the rotor slot number is 44. The rated parameters of both motors are given in Table II.

B. Mechanical Parameters

In order to keep speed constant, a load machine is mechanically coupled to *M1*. Besides, a toothed belt wraps two toothed belt wheels of different diameter mounted on *M1* and *M2*, in contrast to [15]. The experimental test stand is shown in Fig. 5. The belt drive dimensions are given in Table II.

Since the motors are supplied by a single inverter and connected in parallel, they are fed with the same stator voltage and thus share the same electrical speed. Besides, due to the preset belt drive transmission ratio 40/55 (see Table II), scenarios of load imbalance are created as soon as rotor speed is not zero. The presented results (see Figs. 6 and 8) are covering the low speed range where both machines are acting as motor.

The FOC scheme, saliency extraction and torque estimation are programmed in a real-time system from National Instruments. The computational time added by the saliency extraction and torque estimation is approximately 30% compared to dual machine control with four current sensors and two shaft encoders.

VI. EXPERIMENTAL RESULTS

This section shows the experimental results measured at the described test stand. During the experiments, average FOC technique of Fig. 3 is performed. The above-mentioned load motor varies the speed of the *M1* motor. Due to the belt drive, *M2* motor speed differs to *M1* speed. This creates a permanent unbalanced load scenario.

The *M2* stator current phasor acquisition explained in Section-III will be firstly shown. Afterward, motor saliencies and *M2* offset using the strategy proposed in Section-IV will be shown. Finally, encoderless rotor position acquisition will be shown.

The switching sequence used for machine excitation in this article consists of the three sets of antiparallel inverter states: (100&011, 010&101, and 001&110). The excitation time for each active state is 60 μs. Current is sampled at 2 MS/s.

C. Stator Current Phasor Acquisition

This section shows the results of the $\bar{k}$ factor estimation strategy presented in Section III-C. During the experiment of Fig. 6, FOC is carried out by the two induction motors at rated average rotor flux and variable torque. The speed of *M1* is kept constant by the attached load motor at 82.4 r/min. Due to the implemented belt drive, the speed of *M2* results in 60 r/min. Fig. 6(b) shows the computed $\bar{k}$, in terms of amplitude and angle. Fig. 6(c) shows $\psi_{R,M1}$, calculated using two current sensors; $\psi_{R,M2}$, calculated using a single current sensor and the presented current phasor estimation of Section III-B.; $\psi^*_{R,M2}$, calculated using two current sensors (attached to A and B phases, for comparison reasons). The difference $\psi_{R,M2} - \psi^*_{R,M2}$ is also shown. Fig. 6(d) shows T_{M1}, calculated using two current sensors; T_{M2}, calculated using a single current sensor and the presented current phasor estimation of Section III-B.; T^*_{M2},

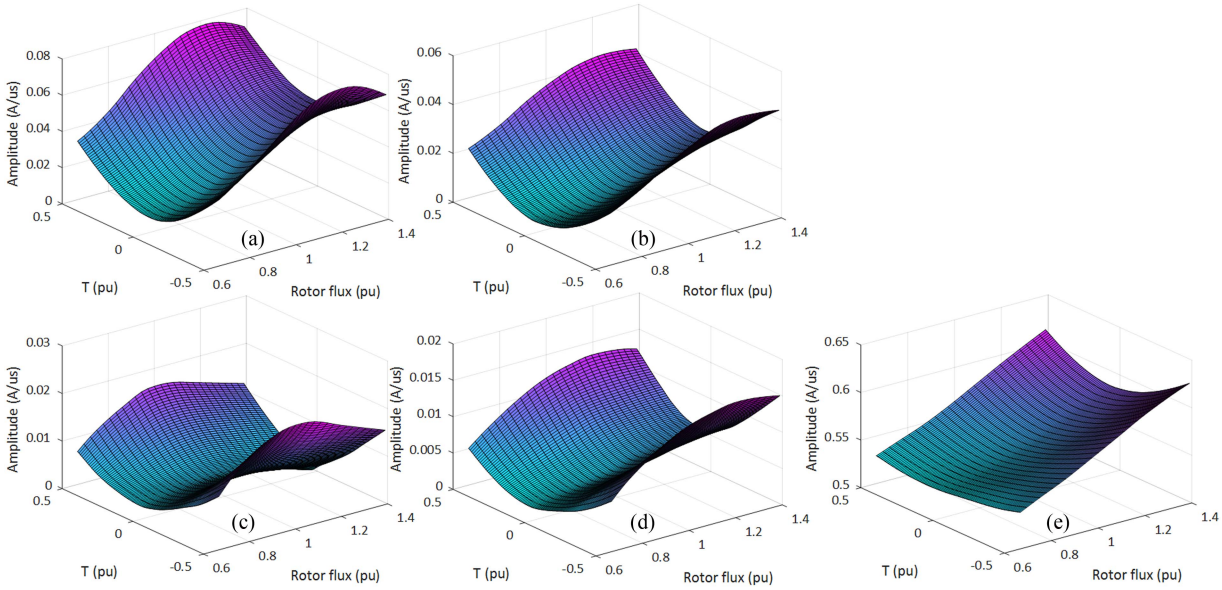

Fig. 7. (a) *M1* saturation saliency amplitude. (b) *M1* intermodulation saliency amplitude. (c) *M2* saturation saliency amplitude. (d) *M2* intermodulation saliency amplitude. (e) *M2* offset amplitude.

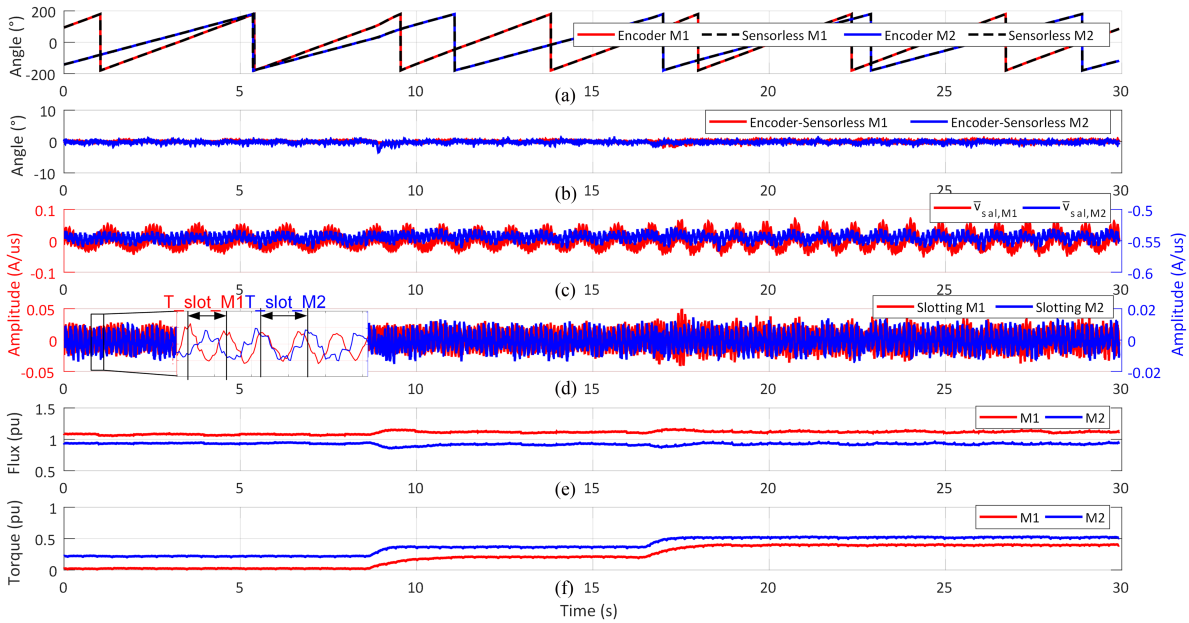

Fig. 8. (a) *M1* and *M2* encoders, and *M1* and *M2* encoderless rotor angles. (b) Rotor angle deviation of *M1* and *M2* (calculated as encoder minus encoderless). (c) Real component of $\bar{v}_{\text{sal},M1}$ and $\bar{v}_{\text{sal},M2}$ calculated as in (19) and (22). (d) Real component of resulting slotting saliency after offset and saliency feedforward compensation using data of Fig. 6. (e) *M1* and *M2* rotor flux. (f) *M1* and *M2* torque.

calculated using two current sensors (attached to A and B phases, for comparison reasons). The difference $T_{M2} - T^*_{M2}$ is also shown. Fig. 6 is not intended to show how the current is exactly distributed in an industrial dual motor application. Yet, it serves as a demonstration of the capability of the proposed method to compute the actual torque and current of each motor.

A scenario of dynamic heavy load imbalance has been shown in Fig. 6. As it can be observed, the proposed current sensor configuration in combination with the presented signal processing successfully computes the torque and flux of both motors, even at *M2* where only one current sensor is available. To guarantee accurate torque-sharing calculation during transients, additional measures will be required.

D. Offset and Saliencies

Fig. 7 shows the saliencies and offset from *M1* and *M2*, calculated as explained in (18) and (21). The amplitudes of

the saturation and intermodulation saliencies, which act as distortions, are plotted in Fig. 7 for multiple flux and torque levels. For the generation of the curves, multiple operating points were measured and an interpolation was carried out. Note that the saliency amplitude of *M2* is approximately three times smaller than that of *M1*, as it was derived in (18) and (21). The saliency amplitudes show a deterministic shape and can thus be eliminated by the mentioned saliency separation method. It is worth to mention that *M1* does not present an offset due to the mathematical elimination shown in (18). It is worth to note that the offset amplitude of *M2* is tenths of times greater than the amplitude of the saliencies.

The phase shift of the rotor-slotting saliency due to motor loading is in this article negligible. As an example, at rated flux, experimental results show that the rotor-slotting angle increases by up to 10 slot degrees (or 10/44 mechanical degrees) when torque is increased from 0% to 50%.

E. Unbalanced-Load Encoderless Operation

During the experiment shown in Fig. 8, the rotor speed of *M1* and of *M2* are kept constant by the attached load motor and belt drive as in previous experiment. It results in *M1* rotating at 13.5 r/min and *M2* at 10 r/min. The control scheme is set to average FOC, where torque points are commanded. The average flux command is set to rated average rotor flux. The average torque command is varied in two dynamic load steps of 15% rated torque. Fig. 8 shows the performance of each motor regarding rotor angle acquisition.

As observed in Fig. 8, a scenario of heavy unbalanced load is achieved resulting from the electrical parallel connection and to the belt drive implemented.

During the whole experiment of Fig. 8, *M1* and *M2* rotor angles are successfully extracted from the corresponding slotting saliencies. The zoomed-in view of Fig. 8(d) shows the resulting rotor-slotting saliency for about 0.5 s. A dominant harmonic (rotor-slotting) is observed, whose period T_slot_*M1* and T_slot_*M2* are shown. The period of the slotting signal is that of the rotor speed divided by N_R. Thus, rotor angle can be computed. The resulting angle deviation, computed as the difference between encoder and slotting-based rotor angle, remains for *M1* within $\pm 1.5°$ and for *M2* within $\pm 3°$.

VII. Conclusion

This article presented an encoderless dual-motor drive that was equipped with three current sensors arranged in a special configuration. Two current sensors were attached to two phases of M1 and the remaining one is attached to one phase of *M2*. A signal processing scheme was proposed to estimate stator current of *M2*, where only one sensor is available. Acquiring *M2* stator phasor is necessary in order to compute flux and torque of *M2*. In addition, a voltage step excitation method was implemented, which extracted rotor-slotting saliency and thus estimated the rotor position of each motor individually. As a result, full encoderless control in the critical operating range around zero frequency/speed could be achieved. By means of the encoderless rotor position and the stator currents phasors of *M1* and *M2*, torque-sharing could be calculated. The proposed drive was tested on a dual induction motor test bench. An implemented belt drive ensured that both motors rotate with a preset gear ratio, producing significant unbalanced load situations. The experimental results showed accurate torque-sharing estimation, which enabled excellent encoderless control performance under heavy unbalanced loads even in the critical operating range around zero mechanical speed.

Acknowledgment

The authors want to thank ALSTOM, especially Mr. H. Mannsbarth (head of Components-Bogies/Drives department in global Rolling Stock Platform/Components division) and Mr. Cedric Zanutti (head of R&D/Technology in RSC-Bogies/Drives) for their generous support, research/development funding and project supervision. Furthermore, the authors want to thank colleagues from ALSTOM group (Mr. Newesely, Mr. Cepak, Mr. Ganster and Mr. E. Moser) for their feedback and great support.

The authors are very indebted to LEM Company (especially Mr. A. Hürlimann/Chairman of Board of Directors and Mr. J. Burk) for cooperation and generous support.

The authors acknowledge TU Wien Bibliothek for financial support through its Open Access Funding Program.

References

[1] F. Xu and L. Shi, "Unbalanced thrust control of multiple induction motors for traction system," in *Proc. IEEE Ind. Electron. Appl. Conf.*, 2011, pp. 2752–2757.

[2] F. Xu, L. Shi, and Y. Li, "The weighted vector control of speed-irrelevant dual induction motors fed by the single inverter," *IEEE Trans. Power Electron.*, vol. 28, no. 12, pp. 5665–5672, Dec. 2013.

[3] L. Guo, Z. Yang, F. Lin, and X. Tu, "Weighted torque current control for high speed train with dual induction motors fed by a single inverter," in *Proc. Annu. Conf. IEEE Ind. Electron. Soc.*, 2015, pp. 2723–2728.

[4] A. Bouscayrol, M. Pietrzak-David, P. Delarue, R. Pena-Eguiluz, P.-E. Vidal, and X. Kestelyn, "Weighted control of traction drives with parallel connected ac machines," *IEEE Trans. Ind. Electron.*, vol. 53, no. 6, pp. 1799–1806, Dec. 2006.

[5] J. Holtz and J. Juliet, "Sensorless acquisiton of the rotor position angle of induction motors with arbitrary windings," *IEEE Trans. Ind. Electron.*, vol. 41, no. 6, pp. 1675–1682, Nov./Dec. 2005.

[6] F. Briz and M. W. Degner, "Rotor position estimation," *IEEE Ind. Electron. Mag.*, vol. 5, no. 2, pp. 24–36, Jun. 2011.

[7] W. Fahrner, M. A. Vogelsberger, and T. Wolbank, "A new technique to identify induction machine rotor parameters during dynamic operation and low speed," in *Proc. IEEE 18th Int. Power Electron. Motion Control Conf.*, 2018, pp. 471–476.

[8] Y. Kuono, H. Kawai, S. Yokomizo, and K. Matsuse, "A speed sensorless vector control method of parallel connected dual induction motor fed by a single inverter," in *Proc. IEEE Ind. Appl. Soc. Annu. Meet.*, 2001, pp. 1218–1223.

[9] J. Nishimura, K. Oka, and K. Matsuse, "A method of speed sensorless vector control parallel -Connected dual induction motors by a single inverter with a rotor flux control," in *Proc. Int. Conf. Elect. Mach. Syst.*, 2007, pp. 600–603.

[10] T. Inoue, K. Azegami, K. Matsuse, S. Ito, and Y. Nakajima, "Dynamic performance of sensorless vector controlled multiple induction motor drive connected in parallel fed by single inverter," in *Proc. Ind. Appl. Soc. Meet.*, 2011, pp. 1–6.

[11] G. Wang, L. Yang, B. Yuan, B. Wang, G. Zhang, and D. Xu, "Pseudo-Random high-frequency square-wave voltage injection based sensorless control of IPMSM drives for audible noise reduction," *IEEE Trans. Ind. Electron.*, vol. 63, no. 12, pp. 7423–7433, Dec. 2016.

[12] C. Y. Yu, J. Tamura, D. D. Reigosa, and R. D. Lorenz, "Position self-sensing evaluation of a FI-IPMSM based on high-frequency signal injection methods," *IEEE Trans. Ind. Electron.*, vol. 49, no. 2, pp. 880–888, Aug. 2013.
[13] P. Landsmann, D. Paulus, and R. Kennel, "Silent and parameter independent hybrid sensorless control for SPMSM based on current oversampling," in *Proc. IEEE Int. Symp. Sensorless Control Elect. Drives Predictive Control Elect. Drives Power Electron.*, 2013, pp. 1–8.
[14] E. R. Montero, M. Vogelsberger, M. Bazant, and T. Wolbank, "Saliency-based speed sensorless control of single-inverter dual induction machines using reduced amount of current sensors," in *Proc. IEEE Energy Convers. Congr. Expo.*, 2020, pp. 5098–5103.
[15] E. R. Montero, M. Vogelsberger, and T. Wolbank, "Sensorless speed control of single-inverter dual motors based on slotting saliency harmonic," in *Proc. IEEE Int. Conf. Ind. Technol.*, 2021, pp. 234–239.
[16] Q. Gao, G. Asher, and M. Sumner, "Sensorless position and speed control of induction motors using high frequency injection and without offline pre-commissioning," *IEEE Trans. Ind. Electron.*, vol. 54, no. 5, pp. 2474–2480, Oct. 2007.
[17] R. Morales-Caporal and M. Pacas, "Suppression of saturation effects in a sensorless predictive controlled synchronous reluctance machine based on voltage space phasor injections," *IEEE Trans. Ind. Electron.*, vol. 58, no. 7, pp. 2809–2817, Jul. 2011.
[18] E. R. Montero, M. Vogelsberger, M. Bazant, and T. Wolbank, "A new approach to detect load sharing of dual-motors driven and controlled by a single converter using only three current sensors," in *Proc. IEEE Int. Conf. Elect. Mach.*, 2020, pp. 1040–1045.

Eduardo Rodriguez Montero (Student Member, IEEE) was born in Leon, Spain. He received the B.Sc. degree in electromechanical engineering from Comillas Pontifical University, Madrid, Spain, in 2015, and the M. Sc. degree in electrical engineering from the Denmark Technical University, Kongens Lyngby, Denmark, in 2017.

Since 2017, he has been a Scientific Research Assistant toward his Ph.D. on sensorless ac machine control with Vienna University of Technology, Vienna, Austria.

Markus Vogelsbergerwas born in Tirol, Austria. He received the Dipl.-Ing. (Hons.) and Dr.Techn/Ph.D. (Hons.) degrees in electrical engineering from Vienna University of Technology, Vienna, Austria, in 2004 and 2009, respectively.

He has been a Scientific Research Assistant with the Institute of Energy Systems and Electrical Drives, TU-Vienna, where he has been engaged in several industrial and scientific R&D projects. He was with Georgia Institute of Technology University, Atlanta/USA for study and research activities in 2006 and 2008, respectively. He started his industrial career with Bombardier Transportation, Vienna, in 2011 and has worked in various positions in engineering and management since then. He is currently with ALSTOM (Bombardier Transportation joined the Alstom Group in 2021) acting as global DRIVES R&D/Innovation and Technology Manager including IPR in Rolling Stock Platform/Components division - Bogies & DRIVES department. He has authored/co-authored more than 85 scientific publications in refereed technical journals and international conferences. His was the Responsible Manager is on research and managing of high innovative topics like speed sensorless drives strategies for traction & road applications, state of the art motor winding insulation and smart condition monitoring of inverter-fed machines & whole propulsion chain. In particular his interests include interdisciplinary & multi objective R&D cooperation projects in the important field of "green-mobility" together with well-known partners from academia and industry. Since 2020, he has been the Convenor of the international standard IEC 60349 (Electric traction - Rotating electrical machines for rail & road vehicles). His fields of interest include traction motors, drive technologies, power electronics and multidisciplinary drives projects.

Thomas Wolbank (Member, IEEE) was born in Carinthia, Austria. He received the Doctoral and Associate Prof. degrees in electrical engineering from Vienna University of Technology, Vienna, Austria, in 1996 and 2004, respectively.

He is currently with the Department of Energy Systems and Electrical Drives, Vienna University of Technology, Vienna. He has co-authored more than 200 papers in refereed journals and international conferences. He is the Chair of the IEEE IES Technical Committee on Electrical Machines (Term 2021/2022). His research interests include saliency-based sensorless control of ac drives, dynamic properties and condition monitoring of inverter-fed machines, transient electrical behavior of ac machines, and motor drives and their components, controlling them by the use of intelligent control algorithms.